LES/RANS MODELING OF AERO-OPTICAL EFFECTS IN A SUPERSONIC CAVITY FLOW

Ilya A. Zilberter
Jack R. Edwards

13 June 2016

Final Report

AIR FORCE RESEARCH LABORATORY
Directed Energy Directorate
3550 Aberdeen Ave SE
AIR FORCE MATERIEL COMMAND
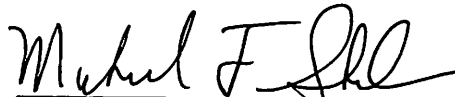**KIRTLAND AIR FORCE BASE, NM 87117-5776**

NOTICE AND SIGNATURE PAGE

//signed//   //signed//
_____   _____
JOHN TAM, DR-III, DAF   MICHAEL F. SHEEHAN, DR-IV
Work Unit Manager   Deputy Chief, Laser Division

REPORT DOCUMENTATION PAGE

1. REPORT DATE *(DD-MM-YYYY)* 13-06-2016	2. REPORT TYPE Final Report	3. DATES COVERED *(From - To)* 13 April 2015- 13 June 2016
4. TITLE AND SUBTITLE LES/RANS Modeling of Aero-Optical Effects in a Supersonic Cavity Flow		**5a. CONTRACT NUMBER** FA9451-15-1-0041
		5b. GRANT NUMBER
		5c. PROGRAM ELEMENT NUMBER
6. AUTHOR(S) Ilya A. Zilberter, Jack R. Edwards		**5d. PROJECT NUMBER**
		5e. TASK NUMBER
		5f. WORK UNIT NUMBER D07N
7. PERFORMING ORGANIZATION NAME(S) AND ADDRESS(ES) North Carolina State University 2701 Sullivan Dr. STE 240 Campus BX 7514 Raleigh NC 27695-7003		**8. PERFORMING ORGANIZATION REPORT NUMBER**
9. SPONSORING / MONITORING AGENCY NAME(S) AND ADDRESS(ES) Air Force Research Laboratory 3550 Aberdeen Ave SE Kirtland AFB, NM 87117-5776		**10. SPONSOR/MONITOR'S ACRONYM(S)** AFRL/RDLE
		11. SPONSOR/MONITOR'S REPORT NUMBER(S) AFRL-RD-PS-TR-2016-0035

12. DISTRIBUTION / AVAILABILITY STATEMENT

Approved for public release. Distribution is unlimited. OPS-16-12188 Jul 1, 2016.

13. SUPPLEMENTARY NOTES

14. ABSTRACT

A hybrid Large Eddy simulation / Reynolds-Averaged Navier-Stokes turbulence model is applied to compute the wavefront aberrations in an optical beam passing through a supersonic open cavity flow. The turbulence model blends a RANS-type closure near solid walls with a subgrid model in the free-stream based on the ratios of estimated inner and outer turbulent length scales. The cavity geometry is modeled using an immersed boundary method, and an auxiliary flat plate simulation is performed to replicate the effects of the wind-tunnel boundary layer on the computed optical path difference. Two-dimensional proper orthogonal decomposition modes of the optical wavefront are computed; these compare favorably with wind tunnel data despite uncertainties about inflow turbulence levels and boundary layer thicknesses over the wind tunnel window. Dynamic mode decomposition of a planar wavefront spanning the entire cavity reveals that wavefront distortions are driven by shear layer oscillation at the Rossiter frequencies; these disturbances create eddy shocklets that propagate into the free-stream and create additional optical path disturbances.

15. SUBJECT TERMS

COIL, Diffuser, LES, RANS

16. SECURITY CLASSIFICATION OF:			17. LIMITATION OF ABSTRACT	18. NUMBER OF PAGES	19a. NAME OF RESPONSIBLE PERSON John Tam
a. REPORT Unclassified	**b. ABSTRACT** Unclassified	**c. THIS PAGE** Unclassified	SAR	31	**19b. TELEPHONE NUMBER** *(include area code)* 505-853-7944

Standard Form 298 (Rev. 8-98)
Prescribed by ANSI Std. 239.18

TABLE OF CONTENTS

Section   **Page**

LIST OF FIGURES

1.0 SUMMARY

This report describes the application of large-eddy simulation / Reynolds-averaged Navier-Stokes (LES/RANS) techniques to simulate supersonic flow over a cavity configuration tested in the Air Force Research Laboratory's (AFRL) Trisonic tunnel. The model is used to compute the wavefront aberrations in an optical beam passing through the cavity. The turbulence model blends a RANS-type closure near solid walls with a subgrid model in the free-stream based on the ratios of estimated inner and outer turbulent length scales. The cavity geometry is modeled using an immersed boundary method, and an auxiliary flat plate simulation is performed to replicate the effects of the wind-tunnel boundary layer on the computed optical path difference. Two-dimensional proper orthogonal decomposition modes of the optical wavefront are computed and compare favorably with wind tunnel data despite uncertainties about inflow turbulence levels and boundary layer thicknesses over the wind tunnel window. Dynamic mode decomposition of a planar wavefront spanning the entire cavity reveals that wavefront distortions are driven by shear layer oscillation at the Rossiter frequencies; these disturbances create eddy shocklets that propagate into the free-stream and create additional optical path disturbances.

It should be noted that the subject discussed in this report is different from that originally proposed, which focused on simulations of the effects of heat release due to lasing chemistry on shock-train formation within chemical oxygen iodine lasers (COILs). A delay in funding (due to the DoD sequester) led to a change in the scope of work, spurred by Ilya Zilberter's stay at AFRL during the summers of 2014 and 2015. Ilya was the Ph.D. student supported under this work. A no-cost extension has been awarded for this work to allow us to complete some of the work proposed under the original statement of work.

2.0 INTRODUCTION

Externally-mounted optical systems (e.g. an aircraft-mounted laser) may experience disturbances in the beam path caused by turbulence or other flow features. In the case of an optical device inside an open cavity, the beam must pass through a turbulent detached shear layer and a series
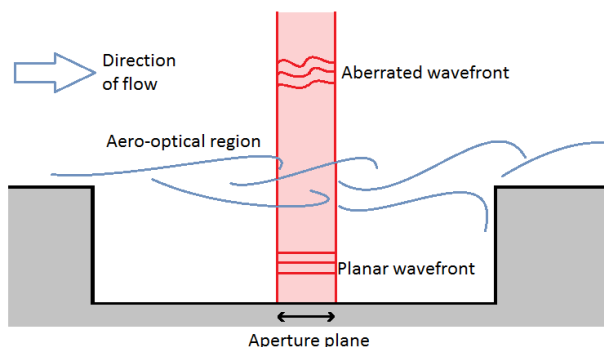
Figure 1. Schematic of cavity flow with optical reflector at bottom of cavity

of acoustic waves which result from flow re-attachment at the back of the cavity, both of which can affect the coherence and power of the beam by aberrating the beam wavefront (Figure 1) When designing such systems, it is important to be able to predict and model these aero-optical effects.

The present study aims to do so using a hybrid Large-Eddy Simulation / Reynolds-Averaged Navier-Stokes (LES/RANS) turbulence closure. This approach directly resolves large turbulent eddies in the free stream while switching over to a RANS model to simulate the smaller-scale eddies near the walls. Thus the simulation should be able to capture the transient, large-scale turbulence structures characteristic of these types of cavity flows while requiring smaller computational meshes than traditional LES. Detached eddy simulation (DES) and LES/RANS methods have been applied to cavity flows in several prior studies, including for both supersonic and subsonic cavity flows, and are generally able to capture the cavity flow physics with good accuracy. Among more recent efforts, Wang, et al. [1] used a hybrid LES/RANS model to simulate a relatively high aspect-ratio cavity in Mach 1.8 and 2.5 free-stream conditions and were able to accurately predict the oscillation frequencies of the shear layer as well as mode switching to more wake-like behavior. Peng and Liecher [2] used a hybrid LES/RANS code to simulate a three-dimensional Mach 0.85 cavity flow including the entire wind tunnel geometry. While their approach managed to capture the first three acoustic disturbance modes, the spectral behavior associated with higher frequencies was not sufficiently resolved, partly due to insufficient resolution of the computational grid and simulation time step.

An advantage of LES and LES/RANS methods is that the direct simulation of large eddy structures allows for the prediction of aero-optical effects, which arise from density fluctuations within the optical path. Mani, et al. [3] argue that the smallest optically-active turbulence scales fall within the range typically resolved in standard LES applications. [4] Morgan and Visbal [5] used a RANS/ (implicit) LES turbulence model to simulate aero-optical aberrations resulting from flow over an optical turret, achieving fair comparison with experimental data over a range of elevation angles, albeit with deviations in the separated flow region behind the turret. Engfer, et al. [6] performed delayed detached-eddy simulations (DDES) of flow around the aircraft-mounted SOFIA telescope but their results were hampered by insufficient turbulence resolution in the inflow boundary layer, which caused computed wavefront aberrations to differ from experimental values by a factor of 4. Additionally, the instrument used to detect spatially-resolved wavefront aberrations in the experiment was out of focus and failed to produce evidence of spatially coherent turbulent structures.

Presently, we examine a supersonic, three-dimensional cavity flow on a high-resolution computational mesh in order to test the capability of LES/RANS models to predict aero-optical phenomena. While most prior studies have used experimental validation in the form of pressure data sampled along the cavity floor and walls or one-dimensional wavefront deflection spectra, recent experiments in the Trisonic Gasdynamic Facility (TGF) [7] at Wright-Patterson AFB have yielded Shack-Hartmann wavefront measurements for a range of supersonic cavity flows that directly show the optical aberrations caused by the detached shear layer. Using these data for validation allows for the comparison of not only the modal frequencies of the optical disturbances, but of their shape as well. Figure 2 shows the cavity geometry within the blocked-out simulation domain. The optical beam is highlighted in red.
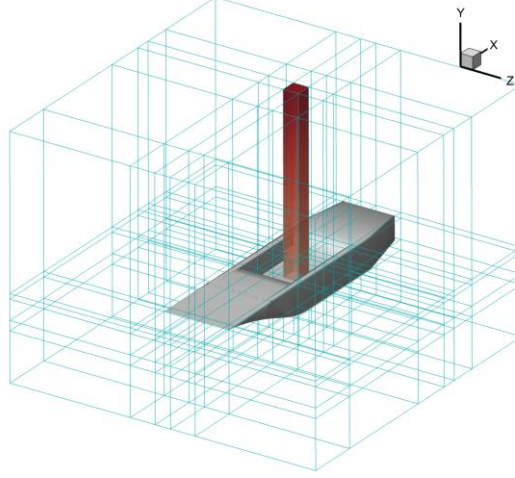
Figure 2. Overview of simulation domain with optical beam path highlighted in red

3.0 METHODS, ASSUMPTIONS, AND PROCEDURES

3.1 Time Advancement

NCSU's REACTMB flow solver is used in the present effort. REACTMB solves the Navier-Stokes equations governing a multi-component mixture of gases on simply-connected, multi-block structured meshes using finite-volume methods. REACTMB is designed for use on massively-parallel computers and uses MPI for message-passing. Large structured meshes are decomposed into a number of smaller blocks, which are then partitioned over the number of requested cores using a simple divide-and-conquer strategy. REACTMB discretizes the Navier-Stokes system in time using a Crank-Nicholson approach:

$$\Omega \frac{U^{n+1,k} - U^n}{\Delta t} + \frac{1}{2}(1+\theta)R(V^{n+1,k}) + \frac{1}{2}(1-\theta)R(V^n) = 0 \tag{1}$$

where Ω is the cell volume, Δt is the time step. U is the vector of conserved variables, and R is the residual vector. The function θ is defined as

$$\theta = \frac{1}{2}(1 - \tanh(\frac{d - d_t}{\Delta d})), \quad d_t = 1 \times 10^{-4} \text{m}, \quad \Delta d = 0.2 d_t \tag{2}$$

Here, d is the distance to the nearest solid surface. The function θ switches the time discretization from Crank-Nicholson to Euler implicit for mesh cells essentially within the laminar sub-layer. Some loss of temporal accuracy results, but this approach is necessary to suppress oscillations in the pressure and transverse-velocity fields for mesh cells with a very high aspect ratio. The matrix system that results from linearizing (1) is solved approximately using a block incomplete lower-upper (ILU) factorization method, and the system is converged to a prescribed tolerance over a sequence of sub-iterations. Jacobian matrix elements are stored over the number of blocks mapped to a particular processor, allowing the "freezing" of the matrix elements and their factorization over the duration of the sub-iterations. This reduces the computational workload significantly.

3.2 Flux Formulation

To sustain turbulence, it is necessary to reduce numerical dissipation significantly. The strategy employed in REACTMB combines a TVD scheme with a fourth-order central difference scheme. Edwards's low diffusion flux-splitting scheme (LDFSS) [8] is used as the Riemann solver. The primitive-variable vector $W = [p_s, u, v, w, T, k, \omega]^T$ is used in the reconstruction. TVD schemes preserve monotonicity, which compromises their ability to resolve small-scale turbulence. One means of alleviating this problem is to blend the monotonicity-preserving left- and right-state values with an averaging operator that leads to a fourth-order central difference, so that the latter is used in regions of high vorticity (boundary layers, shear layers) and the former is used in more 'inviscid' regions, where strong shocks might be present. A function due to Ducros, et al. [9], defined at a mesh cell as

$$f = \frac{(\nabla \cdot \vec{V})^2}{(\nabla \cdot \vec{V})^2 + |\omega|^2 + \varepsilon^2}, \quad \varepsilon = 1 \times 10^{-8} V_\infty / \max(\overline{\Delta x}, \overline{\Delta y}, \overline{\Delta z}) \ , \tag{3}$$

is used for this purpose. Here, the divergence of velocity is compared with the vorticity value. If the latter is much larger (in shear and boundary layers, for example), the function moves toward zero, and in free-stream regions near shocks, the function approaches one. At a particular cell interface i+1/2, we use the function as follows:

$$W_{L,i+1/2} = W_{L,i+1/2}^A + \max(f_i, f_{i+1}, 0.1)(W_{L,i+1/2}^M - W_{L,i+1/2}^A)$$

$$W_{R,i+1/2} = W_{R,i+1/2}^A + \max(f_i, f_{i+1}, 0.1)(W_{R,i+1/2}^M - W_{R,i+1/2}^A) \tag{4}$$

$$W_{L,i+1/2}^A = W_{R,i+1/2}^A = \frac{7}{12}(W_i + W_{i+1}) - \frac{1}{12}(W_{i+2} - W_{i-1})$$

The superscripts M and A refer to the monotonicity-preserving scheme and the fourth-order averaging operator, respectively. This scheme, denoted as LD-TVD for low-dissipation TVD, is used for all LES/RANS calculations presented in this paper. Viscous and diffusive terms appearing in the equation system are discretized using second-order central differences.

3.3 LES/RANS Model

NCSU's hybrid LES/RANS methodology [10] is used as the baseline for the current work. In the LES/RANS model, the effects of anisotropic near-wall eddies are modeled using RANS concepts (Menter's $k-\omega$ baseline model), whereas the larger turbulent eddies away from solid surfaces are captured using a large-eddy simulation method. The shift between the closure models is facilitated by modifying the eddy viscosity field according to

$$\mu_t = \rho\left[(1-\Gamma)\nu_{t,sgs} + \Gamma\frac{k}{\omega}\right], \quad \Gamma = \frac{1}{2}\left(1 - \tanh[15(\frac{1}{\lambda_N^2} - 1)]\right) \tag{5}$$

Here, Γ is a time-dependent blending function that connects the RANS and LES branches and the quantity λ_N is a ratio of outer- to inner-layer turbulence length scales, with the former calculated using both ensemble-averaged and instantaneous turbulence data. Specific definitions are as follows:

$$\lambda_N = g(l_{outer})l_{outer}/l_{inner}, \quad g(l_{outer}) = \min[D_1, \max(1, D_2 \frac{\Delta_{max}}{l_{outer}}\sqrt{\frac{\overline{\omega}}{\omega}})] \tag{6}$$

where

$$l_{outer} = C_N \sqrt{\frac{10\nu\bar{\omega} + \bar{k} + \bar{k}_R}{C_\mu^{1/2}\bar{\omega}\omega}}, \quad l_{inner} = \kappa d$$

The model constants D_1 and D_2 are assigned values of 10 and 0.5, based on calibrations for flat-plate boundary layers. The mesh scale Δ_{max} is taken to be the maximum spacing over all three coordinate directions. This form serves to shift the closure to unsteady RANS when there is no possibility of resolving the largest turbulence length scales. If the maximum mesh scale is selected as the outer-layer scale consistently, then the LES/RANS model behaves similarly to detached-eddy simulation, serving primarily to isolate turbulent boundary layers from massively-separated regions. The quantity $\bar{k}_R$ is the resolved turbulence kinetic energy, calculated via ensemble-averaging as

$$\bar{\rho}\bar{k}_R = \frac{1}{2}(\overline{\rho u_k u_k} - \frac{\overline{\rho u_k}\,\overline{\rho u_k}}{\bar{\rho}}) \tag{7}$$

The quantities $\bar{k}$ and $\bar{\omega}$ are ensemble-averages of the _modeled_ turbulence kinetic energy and specific dissipation rate variables, which are obtained from Menter's model. The use of ensemble-averaged as well as instantaneous data allows the RANS-to-LES transition location to 'float' about a time-mean location that is a function of the ensemble-averaged state of the boundary layer. This enables the blending function to respond more directly to large changes in the turbulence length scales that can result from shock interactions. Ensemble-averages are currently calculated using an exponentially-weighted moving average: $\bar{Q}^n = (1-A)\bar{Q}^{n-1} + AQ^n$ with $A = \Delta t / \tau$. The time scale τ is defined as follows for the cases considered herein:

$$\begin{aligned} \tau &= \min(t, t_{res}), \ t < 4t_{res} \\ &= t - 3t_{res}, t \geq 4t_{res} \end{aligned} \tag{8}$$

where $\tau_{res} = L/u_\infty$ is defined in terms of the length of the domain L and the free-stream velocity u_∞ This form assumes that a statistically-stationary state will emerge after about four residence times

3.4 Immersed Boundary Method

Accurate and affordable LES simulations require fine, isotropic mesh resolution in regions of interest. It is desirable to avoid mesh clustering that extends away from solid surfaces into 'free-stream' or 'free-shear layer' areas – the cells that result are normally anisotropic and can lead to severe time-step restrictions as well as oscillations where the fourth-order central different method is used. The 'boat-shaped' cavity geometry shown in Figure 2 has several sharp edges where different flat surfaces are joined – resolving these with typical structured meshes leads to the problems mentioned above, which greatly degrade the accuracy and efficiency of the flow solver. Attempts were made to generate body-fitted meshes using both GridPro and GridGen, but a successful rendering could not be obtained. Instead, we opted to utilize NCSU's established immersed-boundary method [11-13] to mimic the effects of the object on the surrounding flow. A 220 M cell Cartesian mesh containing isotropic cells of sizes no greater than 0.2 mm in the region of interest (the boat-tail geometry and its cavity) was generated, the boat-tail geometry rendered as a stereolithography (STL) file, and procedures

described in [11] and [12] used to 'embed' the object into the computational domain. The 'embedding' process involves first the calculation of the signed distance from any mesh cell to the nearest point on the STL rendering. Cells inside the object are classified as 'interior' cells – fixed properties are enforced for these cells and they do not interact with other cells in the domain. Cells outside the object but with no face, edge, or vertex neighbor inside the object are classified as 'field' cells – the compressible Navier-Stokes equations are solved in these cells. Cells outside the object but with at least one face, edge, or vertex neighbor inside the object are called 'band cells' – here, flow properties are reconstructed based on the external field-cell solution and on the prescribed boundary conditions at the embedded surface.

The following first-order accurate closures are used for the fluid properties in the band cells, where the subscript 'I' indicates properties obtained at an interpolation point located along the normal line extending outward from the nearest surface location corresponding to the band cell in question, and the subscript "B" indicates the band-cell.

$$p_B = p(d_I)$$

$$u_{B,i} - u_{S,i} = u_{T,i}(d_I)\left(\frac{d_B}{d_I}\right)^k + u_{N,i}(d_I)c(\rho, d_I, d_B),$$

$$u_{N,i}(d_I) = (u_j(d_I) - u_{S,j})\mathbf{n}_j\mathbf{n}_i,$$

$$u_{T,i}(d_I) = (u_i(d_I) - u_{S,i}) - u_{N,i}(d_I)$$

(9)

In these expressions, $\mathbf{n}_i$ is the normal vector at the closest point on the body surface, d is a distance from the nearest surface point, $u_{S,j}$ is the velocity at the nearest surface point, and k is a power-law. The choice of k allows the model to replicate a turbulent velocity profile ($k=1/7$ or $1/9$) or a laminar profile ($k=1$). To obtain the temperature distribution near the surface, Walz's relation for the temperature distribution within a compressible boundary layer is used:

Isothermal wall:

$$\frac{T_B}{T(d_I)} = \frac{T_w}{T(d_I)} + \left(1 - \frac{T_w}{T(d_I)} + \frac{r(\gamma-1)}{2\gamma RT(d_I)}[u_{T,i}(d_I)]^2\right)\left(\frac{d_B}{d_I}\right)^k$$
$$- \frac{r(\gamma-1)}{2\gamma RT(d_I)}[u_{T,i}(d_I)]^2\left(\frac{d_B}{d_I}\right)^{2k}$$

(10)

Adiabatic wall:

$$\frac{T_B}{T(d_I)} = 1 + \frac{r(\gamma-1)}{2\gamma RT(d_I)}[u_{T,i}(d_I)]^2(1-\left(\frac{d_B}{d_I}\right)^{2k})$$

(11)

In this, r is the recovery factor and $[u_{T,i}(d_I)]^2$ is the kinetic energy associated with the tangential velocity component at the interpolation point. The function $c(\rho, d_I, d_B)$ that scales the normal velocity component in Eq. (9) is determined by enforcing a discrete form of the continuity equation at each band cell using a locally-parallel flow assumption. Details are given in Ghosh et al. [13]

The turbulence variables in the band cells are defined as

$$k_B = u_\tau^2 / \sqrt{C_\mu} \quad, \omega_B = u_\tau / (\sqrt{C_\mu} \kappa d_B): \quad d^+ > 10.934$$

$$k_B = k(d_I) \left(\frac{d_B}{d_I} \right)^2, \ \omega_B = 60 \nu_w / (0.075 d_B^2): \quad d^+ < 10.934 \tag{12}$$

$$d^+ = u_\tau d_b / \nu_w, \quad u_\tau = |u_{T,i}(d_I)| / (\ln(d^+) / \kappa + 5.1)$$

(iterative solution)

To arrive at this form, we assume equivalence between the result provided by the power-law profile and the law of the wall within the band cells. Details regarding the calculation of flow properties at the 'interpolation point' may be found in [11-13].

3.5 Optical Path Difference Calculations

Optical Path Difference (OPD) data from the physical experiment at the TGF is provided by a 3cm diameter laser beam which is reflected off of the bottom of the cavity and into a Shack-Hartmann wavefront detector outside of the wind tunnel. The OPD at each point on the detector is related to the Optical Path Length (OPL),

$$\text{OPD}(x,z,t) = \text{OPL}(x,z,t) - \overline{\text{OPL}(x,z,t)} \tag{13}$$

which in turn is proportional to the integral of the gas density in the beam path,

$$\text{OPL}(x,z,t) = \int_a^b \left[K_{GD} \rho(x,y,z,t) + 1 \right] dz \tag{14}$$

where ρ is the density and K_{GD} is the Gladstone-Dale constant (2.27×10^{-4} m^3/kg for visible light in air). Time-accurate density data from the LES/RANS simulations can be used to reconstruct the simulated OPD along a virtual beam path and directly compared with sensor data from the physical experiment. To this end, path integrals of the density along a 3-cm wide region above the center of the simulated cavity are sampled at a rate of 24 kHz as in the physical experiment. Each integral is then processed to convert the density into an OPD snapshot according to Eqs. 13 and 14. The OPD is further processed to remove the tip and tilt components of the wavefront which represent the average gradients of OPD in the two directions across the aperture. Traditionally, this is done in experimental studies to remove the effects caused by vibrations in the wind tunnel or optical instruments, which would cause mono-directional deflections in the measured wavefront. However, it is understood that some flow features introduce tip and tilt components that do not fall under experimental error [7]. For example, the thickening of a boundary layer across the aperture causes a significant tilt in the wavefront. Nonetheless, even though OPD data from the LES/RANS simulations is free of instrumentation error, the tip and tilt components are still filtered out for the sake of comparison with experimental results. This is done by minimizing a target function G over the aperture Ap [4]:

$$G = \iint_{Ap} \left[\text{OPL}(x,z,t) - (Ax + Bz + C)^2 \right] dxdz \tag{15}$$
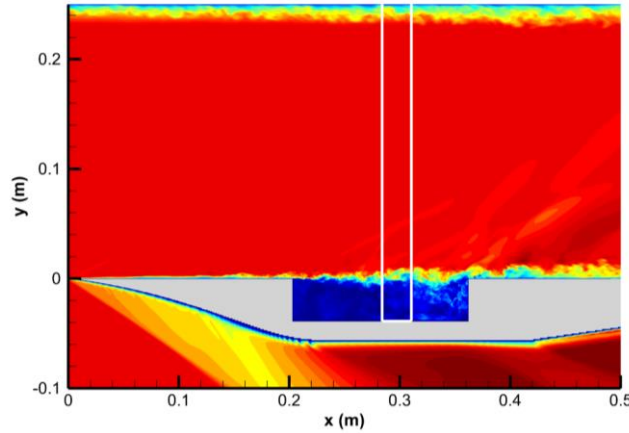
Figure 3. Superimposed LES/RANS centerline snapshots of cavity and wind tunnel wall domains. Optical path outlined in white

Solving $dG/d(A,B,C)=0$ fits a linear OPL wavefront to the actual data in a least-squares sense. The tip/tilt-removed OPD is then given by:

$$\text{OPD}(x,z,t)=\text{OPD}(x,z,t)-(Ax+Bz+C) \qquad (16)$$

where $(Ax+Bz+C)$ represents a linear OPL function and implicitly includes the aperture-averaged OPL term in Eq. 5. In a sense, this tip/tilt removal procedure is a basic form of adaptive optics that results in a zero-mean OPD wavefront that only includes higher-order aberrations.

Because the top wall of the wind tunnel is not modeled in the cavity simulation, a separate turbulent boundary layer simulation with identical free-stream conditions was performed on a 4 million cell mesh to account for the effect of turbulence along the wind tunnel window on the beam. A superimposition of simulation snapshots along both the cavity and boundary layer centerlines is shown in Figure 3, with the Shack-Hartmann beam location outlined in white to highlight the turbulent regions that the beam passes through. The boundary layer thickness of 18mm and *rms.* OPD levels are compared to empty wind tunnel data given in Ref. [7] for validation, and the density integral along the beam path is added to that of the cavity simulation when computing the total OPD.

4.0 RESULTS AND DISCUSSION

4.1 Flow Structure

The LES/RANS cavity and boundary layer flow simulation were initialized from a converged RANS solution and progressed for approximately 35 cavity flow-over times, yielding both instantaneous and time-averaged flow data which are useful in giving an overview of the overall flow dynamics. Figure 4 compares a Schlieren photography snapshot from the physical experiment with instantaneous density gradient $(\partial\rho/\partial y)$ contours along the centerline of the simulation domain. Overall, the LES/RANS captures the broad structure of flow over the body. The angles of the oblique shocks at the splitter tip and cavity edge are well-replicated, as is the region of shed shocklets above the shear layer spanning the cavity. These are caused by the high-speed free-stream air flow impacting slower-moving eddies as they rise above the shear layer.
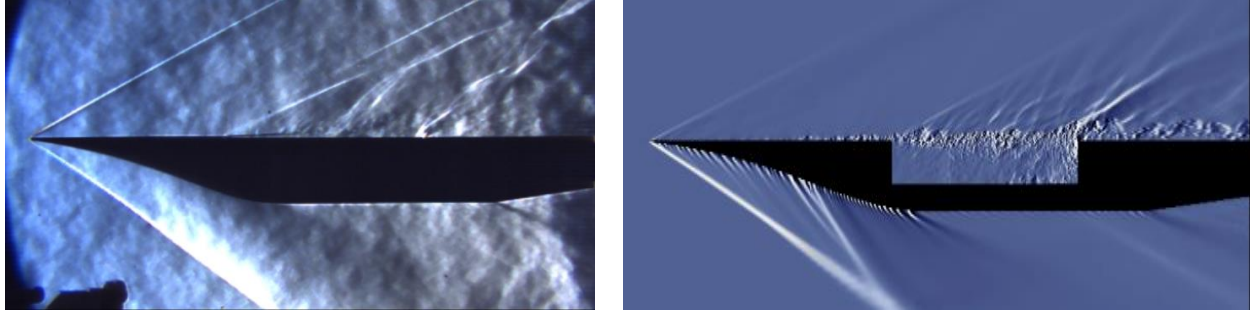
Figure 4. Schlieren snapshot of domain. Left: experiment. Right: LES/RANS centerline

The 'wave'-like shock emanating from the rear cavity wall is also present and is a product of the unsteady impingement of the shear layer on the rear wall. As desired, the geometry of the body creates a turbulent shear layer upstream of the cavity without the need for artificial fluctuations. In the LES/RANS snapshot, the oblique shocks above the body appear to lose strength towards the top of the domain because of numerical dissipation caused by larger cell sizes towards the top boundary. The contraction region underneath the body also exhibits a noticeable 'stair-stepping' effect due to the IB method attempting to resolve a curved surface using rectilinear cells. This effect is a drawback of enforcing full mass conservation within the 'band cells'. Although this is not ideal, the flow underneath the body does not affect conditions near the cavity itself and so the effect was not considered important.

Figure 5 shows the instantaneous density and stream-wise velocity contours at the cavity centerline. The shear layer rapidly thickens and develops very fine turbulent structure but has enough energy to span the cavity without significant deflection. Based on the high level of small-scale density fluctuations in the shear layer, it can already be expected that this region of the flow
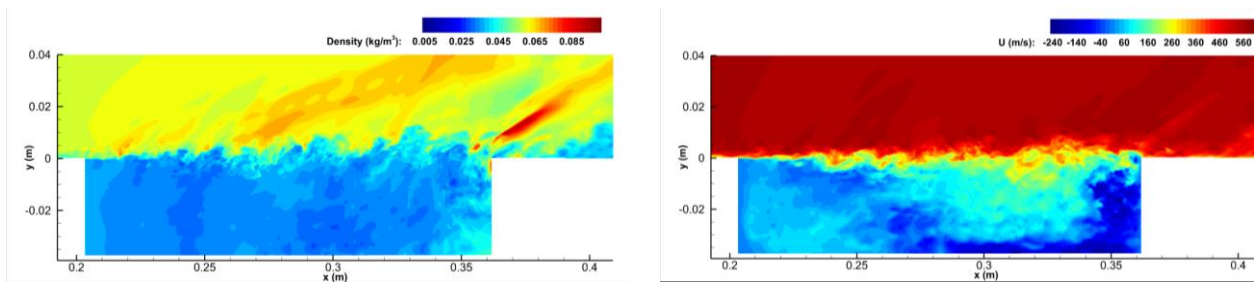
Figure 5. Centerline snapshot of cavity from LES/RANS simulation. Left: density contours. Right: streamwise velocity contours

will produce the most aero-optical aberrations in the path of the beam. Significant, but larger-scale, density variations are also seen above the shear layer in the region of shed shocks. In the density snapshot, a density wave can be observed inside the cavity at x=0.25m. As the wave travels upstream and hits the front cavity wall, it will create a deflection in the shear layer that propagates the shear layer oscillation cycle.

The centerline velocity contour (Figure 5) reveals a strong region of reversed flow in the downstream half of the cavity, especially at the aft wall and along the cavity floor. The flow in the cavity is actually divided into four distinct recirculation zones which are symmetric about the centerline. The strong reversed flow at the aft wall caused by the shear layer impingement moves along the cavity bottom and feeds into the two vortices in the upstream corners; the air in these zones then rises until it is entrained by the shear layer and carried either out of the cavity or into

the two downstream vortices. The complexity of this flow structure compared to the single recirculation zones normally predicted in two-dimensional cavity simulations highlights the need to consider this class of problems as fully three-dimensional.

Finally, Figure 6 shows an instantaneous density isosurface near the top of the shear layer to help visualize the some of the turbulence structure in the optical path (shown in red). As the shear layer detaches from the front cavity wall, it is largely two-dimensional in nature. However, by the time the flow encounters the beam path it has devolved into large, uncorrelated, three-dimensional eddies. The largest of these spans about half of the beam width; the aero-optical data from the virtual Shack-Hartmann sensor should therefore reflect all or most of the turbulent scales in the flow, although not necessarily all of the larger–scale flow dynamics.
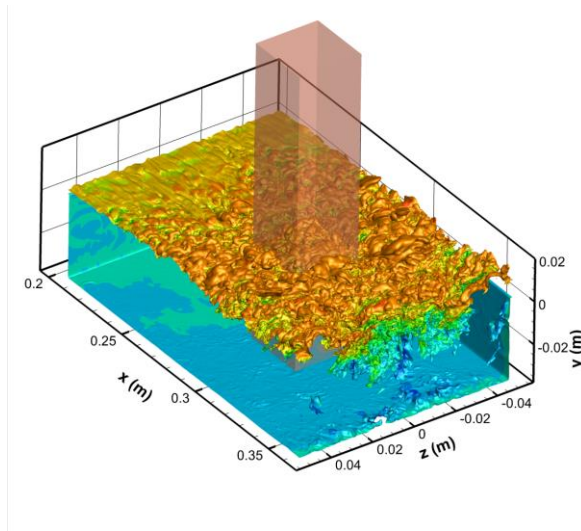
Figure 6: Instantaneous density isosurface above cavity colored by streamwise velocity. Optical path shown in red.

4.2 Cavity Spectral Behavior
.

In order to quantify the oscillations of the shear layer, wall pressures along the cavity line were sampled at 500kHz and processed into pressure spectra. Figure 7 shows pressure spectra at the center of the front and rear cavity walls. The dotted lines denote the dominant frequencies predicted by the empirical Rossiter formula [14]
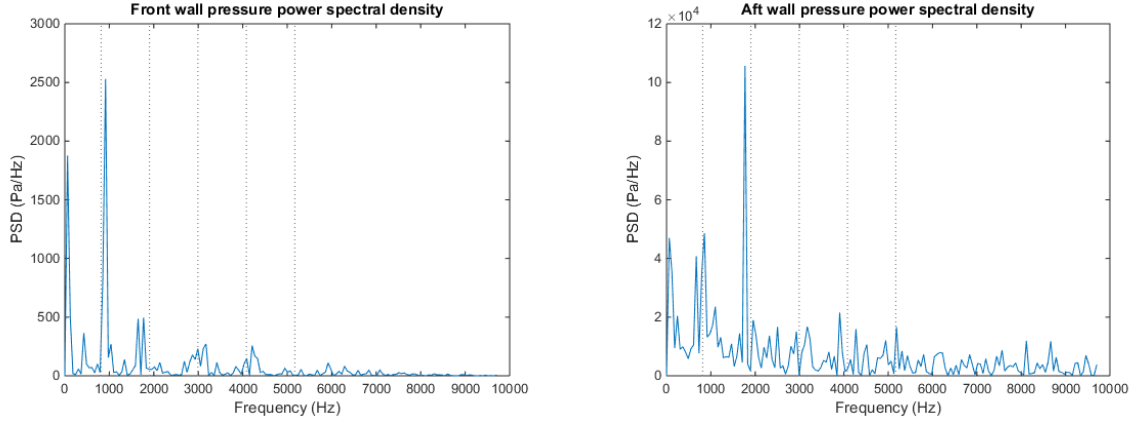
Figure 7. Power spectral density at center of front and rear cavity lip. Dotted lines show first five oscillation frequencies predicted by Rossiter's formula.

$$f_m = \frac{U_\infty}{L}\left[\frac{m - 0.25}{M_\infty\left(1 + \frac{\gamma-1}{2}M_\infty^2\right)^{-1/2} + \frac{1}{0.58}}\right] \tag{17}$$

where m is the mode number, U_∞ and M_∞ are the free-stream velocity and Mach number, and L is the cavity length. Table 1 lists the first five Rossiter modes for this cavity. For both locations, the dominant frequencies closely align with the Rossiter modes, with the front wall displaying first mode dominance and the rear wall aligning with the second mode. At both stations, a significant low-frequency component is observed. This is likely due to transitions to 'wake mode' behavior, which is caused by the boundary layer upstream of the cavity intermittently detaching and shedding a large vortex. Wake mode behavior has been observed in both numerical [15] and experimental [16] studies of similar cavities at supersonic flow conditions. Overall, the spectral data agree very well with both the empirical oscillation frequencies and the behavior seen in prior studies.

Table 1. First five Rossiter frequencies based on Eq. 17

Mode number	Frequency (Hz)
1	816
2	1904
3	2993
4	4081
5	5170

4.3 Aero-Optical Analysis

Density data from cells along the beam was sampled every 208 iterations (equivalent to 24 kHz, which is the sampling rate of the Shack-Hartmann detector) and used to compute the OPD according to Eqns. 13-16. In order to include the effects of the wind tunnel wall in the cavity simulation, the density integrals from the boundary layer and cavity simulations were linearly added before computing the OPD. The resulting path length was greater than the distance between the cavity and tunnel wall in the experiment; however, this included a large laminar free-stream region which contributed nothing to the OPD when the average OPL was subtracted from the solution as in equation 4. In effect, the total length of the beam is arbitrary when computing the OPD as long as the optically active regions of flow (i.e, regions containing turbulent eddies or shock waves) are included in the path. The cross-section of the 3cm beam was resolved in 30×30 cells in the boundary layer simulation and 120×120 cells in the cavity

simulations. When computing the joint OPD, the cavity data was interpolated onto the coarser grid. This was still sufficient resolution for experimental validation as the Shack-Hartmann detector resolved the beam using 32×32 apertures. Subsequent analysis of OPD from the cavity simulation that excludes the wall boundary layer is performed on snapshots with the original 120×120 resolution.

A comparison of the OPD data from the LES/RANS simulation and physical experiment is given in Figure 8. Subfigure (a) shows an instantaneous snapshot of the tip and tilt removed OPD from the simulation. The time-averaged mean OPD has also been removed, resulting in a snapshot capturing the unsteady, higher-order aberrations. Higher values of OPD indicate regions of the beam that passed through higher density areas and experienced a relative phase delay. High levels of disturbances in the wavefront can be observed and are a direct reflection of turbulent eddies in the beam path. Figures 8(b) and 8(c) compare the RMS values of the mean/tip/tilt removed OPD, calculated as:

$$\text{OPD}_{RMS} = \frac{1}{N}\sum_{i=1}^{N}\sqrt{\text{OPD}_i - \text{OPD}_{mean}}, \quad \text{OPD}_{mean} = \frac{1}{N}\sum_{i=1}^{N}\text{OPD}_i \qquad (18)$$

where N is the total number of OPD snapshots. Overall, the structure of OPD variance in the aperture is well-replicated in the simulation, barring a region of higher phase delay in the center of the aperture in the experiment. There is no ready explanation for the discrepancy, although it could be due to wind tunnel effects. The computed OPD_{RMS} levels are also as much as 20% locally higher than the experimental values. Commonly, an ensemble-averaged value of OPD_{RMS} over the aperture is computed to provide a scalar measure of optical distortion:

$$\text{OPD}_{RMS,S} = \frac{1}{N}\sum_{i=1}^{N}\left[\frac{1}{M-1}\sum_{j=1}^{M}\left(\text{OPD}_{i,j} - \text{OPD}_{mean,j}\right)^2\right]^{1/2} \qquad (19)$$

where M is the number of sub-apertures in each snapshot. The values of $\text{OPD}_{RMS,S}$ for the full optical path, as well as the isolated wall boundary layer and cavity simulations, are given in Table 2. The levels of distortion caused by the tunnel boundary layer are half that of the combined flow, although still significant. The computed value of 7.30 nm for the boundary layer

(a)   (b)   (c)
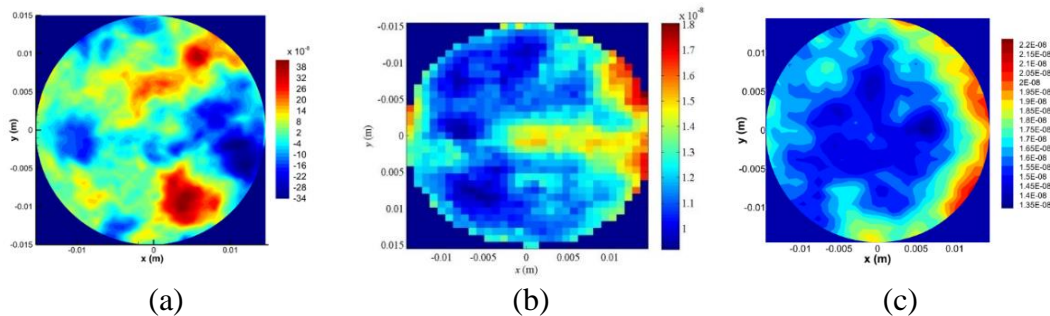
Figure 8. OPD levels along beam path. (a) RMS OPD from experiment. (b) RMS OPD from LES/RANS simulation. (c) Snapshot of mean, tip, and tilt –removed OPD from simulation

is slightly lower than the experimental value of 8.0 nm presented in [7]. At the time of writing the experimental $\text{OPD}_{RMS,S}$ values for the cavity flow were not available; however, due to the

overall higher-than-expected levels of OPD$_{RMS}$ seen in the LES/RANS data in Figure 8, it is expected that the values from the simulation are moderately higher than those of the experiment.

Table 2. Computed OPD$_{RMS,S}$ values over aperture

| Domain	OPD$_{RMS,S}$ (nm)
Combined cavity and wind tunnel wall	14.19
Wind tunnel wall only	7.30
Cavity only	12.07

4.4 Proper Orthogonal Decomposition analysis of OPD

To better understand the turbulent structure driving the optical aberrations, the snapshots of OPD sampled over the course of the simulation can be decomposed into proper orthogonal (POD) modes. POD analysis has widely been used in studies of both aero-optics [7,17] as well as generalized fluid flows [18]. Each spatial mode is a basis function that approximates the variation in the wavefronts in a least-squares sense. Once the POD for a flow has been calculated, each snapshot can be reconstructed using a linear superposition of the modes. The POD modes in this study are computed using Sirovich's method of snapshots [19,20]

The main advantage of the POD is that the flow can be reconstructed using a selected number of orthogonal modes that represent a progressively smaller portion of the overall variance. The first mode is equivalent to the best least-squares approximation to the wavefront variations, the second mode is the second-best representation, and so on. POD modes can be used to form reduced-order models of the flow by projecting the governing equations onto them [18]. They are also potentially useful in adaptive optics applications, since they provide lenslet array shapes that would counteract the largest aero-optical effects [21]. In the present case, the POD modes of the wavefront in the beam serve two purposes. First, the POD modes of OPD from the LES/RANS simulation can be directly compared to those for the experimental data, providing a statistical comparison of measured and computed aero-optical aberrations. Second, the POD modes reveal the size and distribution of coherent structure in the aperture, essentially identifying turbulent structures in the flow. However, the POD does not produce information about the actual flow dynamics, since each POD mode contains information over the full temporal spectrum.

Figure 9 shows the first 10 POD modes of the mean, tip, and tilt-removed OPD from the experiment and simulation. The first POD mode in the experimental data is not well-captured by the simulation. However, there is excellent agreement in the subsequent modes when the simulated modes are 'shifted' by one so that simulated mode 1 corresponds with experimental mode 2, etc. The correlation is flipped somewhat in modes 6-8, with simulated mode 6 matching closely with experiment mode 8, 6 with 5, and 8 with 7. Note that the modes are ordered by eigenvalue magnitude, and some mode swapping can be expected if the eigenvalues (representing total variance contribution of the mode) are close enough. In the simulated decomposition, all three of the modes in question each account for approximately 5% of the total variation in OPD.

It is likely that the discrepancy between the experimental and simulated optical aberrations is due to the peculiarity of the wall boundary layer in the TGF. It is noted in Smith, et

(a) Experiment data

(b) LES/RANS data
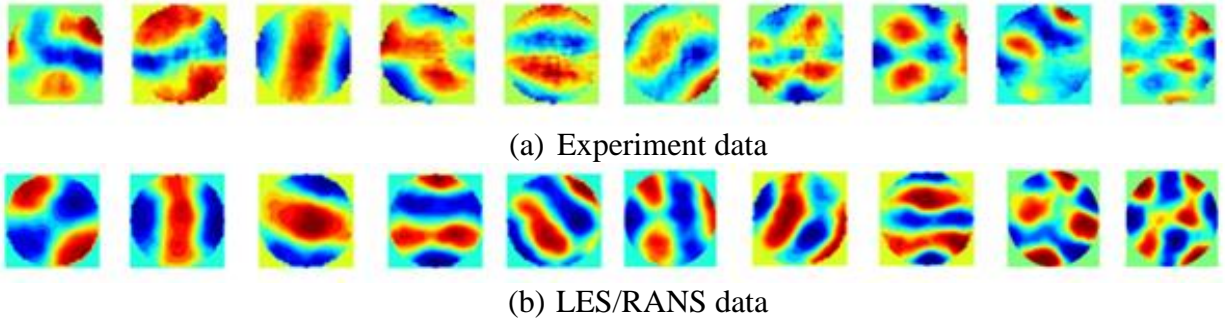
Figure 9. First 10 spatial POD modes of optical path difference through cavity flow and wind tunnel wall boundary layer

al [7] that the boundary layer along the wall in question is tripped somewhere upstream of the test section and therefore might display some wake-like behavior that would influence the optics.

A comparison of the experimental and simulated decomposed OPD modes for the isolated boundary layer is given in Figure 10. Modes 1 through 3 and 6 through 10 show very


(c) Experiment data

(d) LES/RANS data
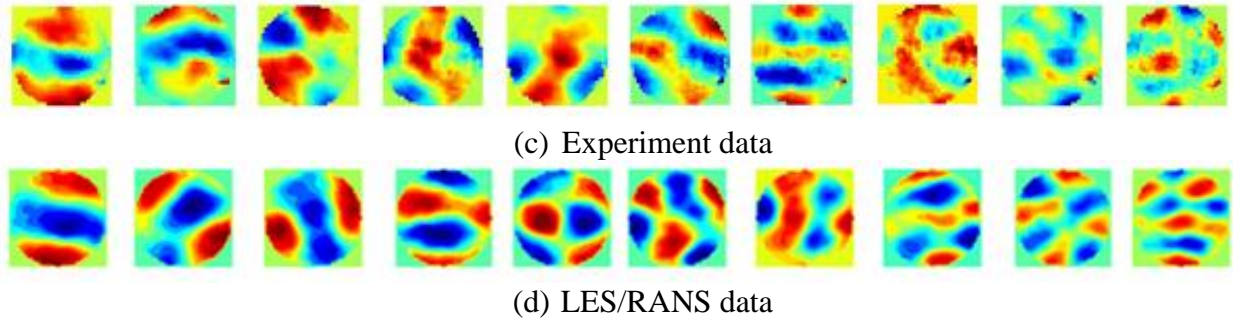
Figure 10. First 10 spatial POD modes of optical path difference through wind tunnel wall boundary layer

good agreement with the experiment, with the caveat that the ordering of the 7th and 8th modes in the simulation is reversed. The fourth and fifth modes of the experiment are not captured by the simulation and are likely unique to the semi-tripped boundary layer found in the experimental facility. In particular, the shape of mode 4 of the experimental boundary layer data is very similar to the first mode of the cavity data and could reflect the same turbulent structure. It is unclear why this feature appears to be more prominent in the cavity flow than the boundary layer flow, or why the LES/RANS simulation is better able to capture the first POD mode of the tunnel wall boundary layer. It is possible that the tripped boundary layer in the wind tunnel forms a trapped-mode resonance when the cavity apparatus is placed in the tunnel; this could potentially amplify any errant structure in the flow. The deviation could also be due to a free-stream disturbance in the wind tunnel that propagates into the interrogation region.

It is interesting to note the apparent similarity between the OPD modes for the boundary layer and cavity flows. In Figure 11, the first ten OPD modes from the two LES/RANS simulations are presented together for comparison, along with the modes of OPD from the isolated cavity flow (with the wall boundary layer omitted from the beam path). Taking mode reordering into account, nine out of ten modes of the boundary layer and isolated cavity flow display a similar structure, with mode 5 being the exception. For better clarity of comparison, the color map of some of the boundary layer modes has been reversed - because the modes are basis functions, their sign is arbitrary. The comparison indicates that a main driving factor behind the

optical aberrations in both flows is the fine eddy structure in the shear layer and boundary layer. The filtering procedure to remove the tip and tilt components from the OPD snapshots removes most of the influence of boundary layer and shear layer thickening, as well as some shear layer structure which is larger than the aperture diameter. Much of the higher order fluctuation that remains is mostly a function of the free-stream Mach and Reynolds number, which explains the agreement in the higher boundary layer and cavity modes. On the other hand, the large aero-optical structures due to the cavity oscillation dynamics are at least somewhat reflected in the cavity data and likely cause the marked deviation of the first three POD modes. A plot of the cumulative modal variance contribution (Figure 12) shows that the boundary layer POD is less compact, indicating that more of the variation in the cavity flow data is due to the lower, larger spatial modes.
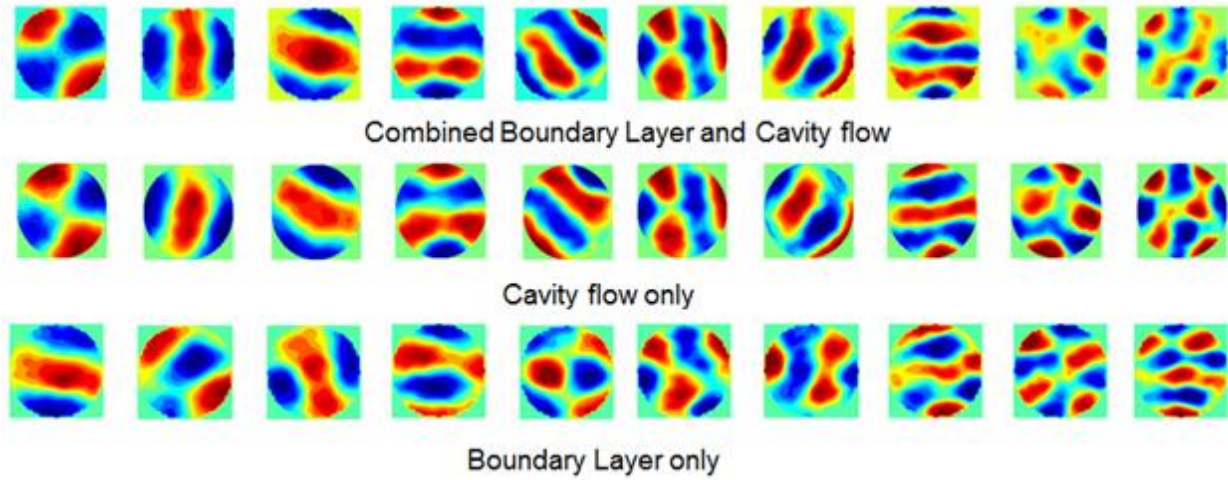
Figure 11. Comparison of first ten OPD modes of isolated cavity flow and wind tunnel wall boundary layer flow
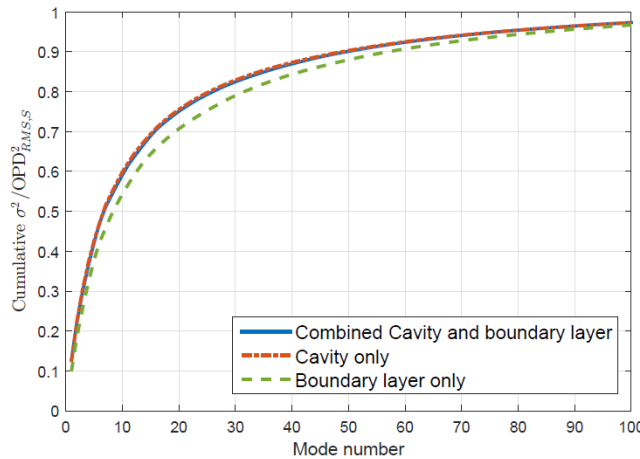

Figure 12. Cumulative modal variances as a fraction of overall wavefront variance

4.5 Contribution of Various Flow Regions

It is of interest to determine the aero-optical contributions of different turbulent regions within the flow, since this is information that cannot easily be determined from the path-integrated OPD data measured in the experiment. An estimate of the OPD contribution along the beam can be obtained from the root mean square density, $(\overline{\rho^2} - (\overline{\rho})^2)^{1/2}$, which is plotted along the cavity centerline and along the beam center in Figure 13. The highest levels of density variation are in the shear layer, with a strong clustering towards the re-attachment point on the aft cavity wall. However, the density fluctuations also appear significant both above and below the shear layer. Inside the cavity itself, the *rms* density rises near the bottom surface, suggesting that there could be some influence from the boundary layer formed by reversed flow circulating upstream from the shear layer impingement point.

The turbulent portions of the flow can be divided vertically into three distinct regions: the recirculation zone within the cavity, the shear layer, and the region of small shocks above the shear layer. The vertical extent chosen for these three regions within the optical path is shown in Table 3. The shear layer region was chosen to be thicker than the actual shear layer to provide a buffer that accounts for shear layer oscillation. The OPD was computed for the section of the beam passing through each of the three regions and broken down by POD as before. A diagram of the beam split into the three regions, along with the first nine POD modes from each region, is presented in Figure 14. As expected, the OPD in the shear layer shows evidence of much finer turbulent structure which shows up as noise in the POD modes, indicative of the small-scale eddies generated in the layer. The two most energetic modes of the shock and shear layer regions are similar in shape and determine the first modes of the full line of sight. The cavity region also exhibits these modes, but in reversed order. A correlation between modal shapes is expected since
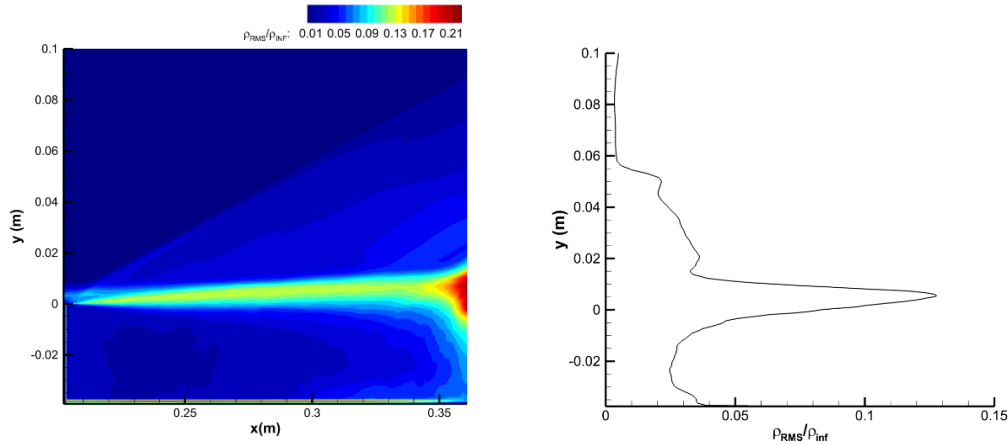
Figure 13. Normalized density variance from LES/RANS simulation. Left: Centerplane of cavity region. Right: Centerline of optical path
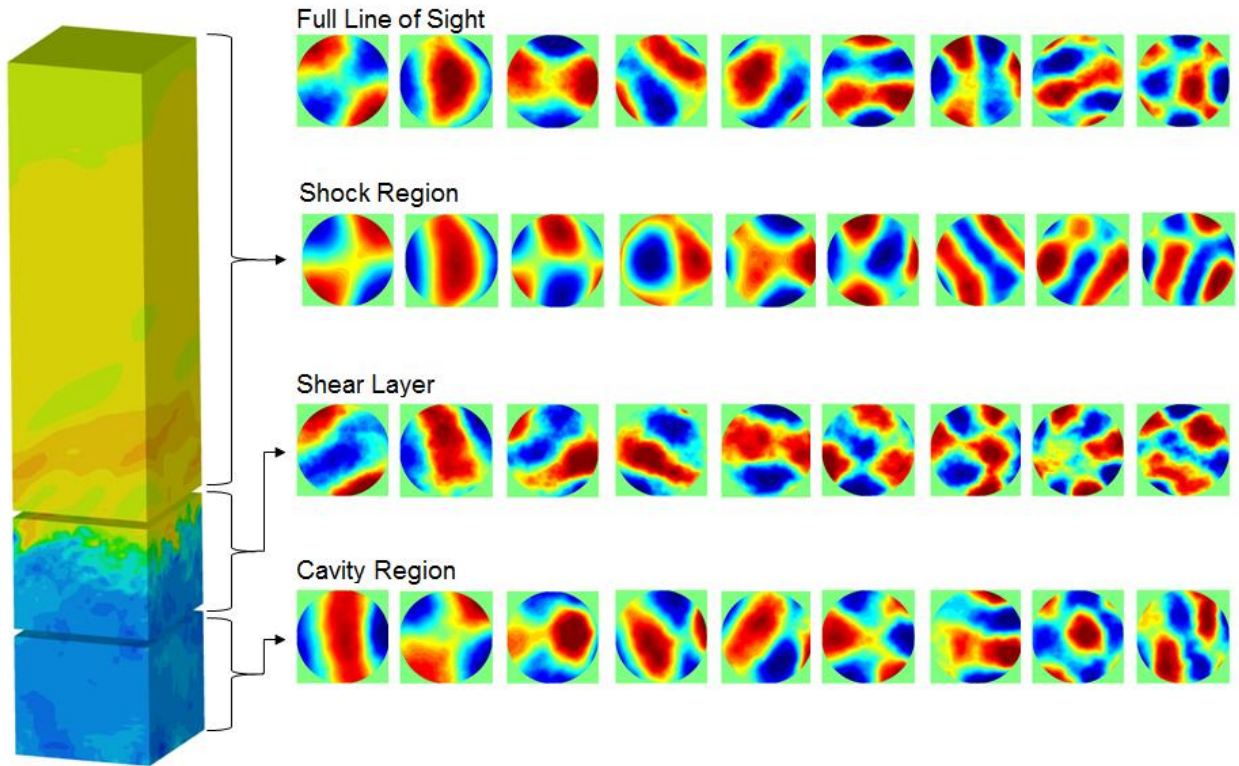
Figure 14. First 9 OPD modes for different flow regions within optical path. Density snapshot along beam shown on left.

Table 3. Extent of distinct flow regions within optical path; cavity lip located at y=0

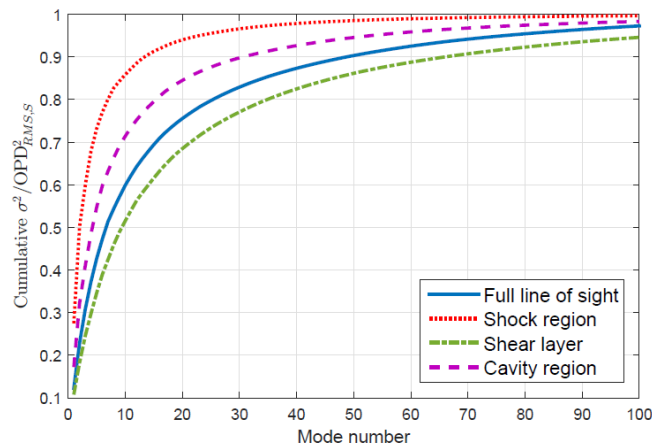| Region	y_{min} (m)	y_{max} (m)
Cavity	-0.037	-0.013
Shear Layer	-0.013	0.01
Shock	0.01	0.1

Figure 15. Cumulative modal variances as a fraction of overall wavefront variance for different flow regions

Table 4: Computed OPD$_{RMS,S}$ values for different flow regions within optical path

Region	OPD$_{RMS,S}$ (nm)
Full line of sight	14.19
Shock Region	2.97
Shear layer	10.34
Cavity region	3.10

the shear layer is ultimately the driver of density variations in the other two regions. The small shock waves in the shock region are generated by the mean flow encountering large eddies on the upper shear layer surface, while part of the cavity region turbulence is generated by air entrained by those same downstream-traveling vortices. The structure of the last three modes in each region begins to show large differences; this is perhaps indicative of the devolution of large eddies in the shear layer into smaller structures, which does not occur (to this degree) in the other two regions.

The modal variance distribution (Figure 15) indicates that the shock region POD is by far the most compact, with the first 10 modes contributing 85% of the total variance. On the other hand, the shear layer variance curve is similar to that of the wall boundary layer, achieving 90% only at the first 60 modes. While the wavefront distortions in the shear layer reflect a broad range of turbulent spatial scales, the shock region exhibits regular, largely coherent structure. Despite the fact that the total OPD$_{RMS}$ contribution of the shock region (Table 4) is one third of that of the shear layer, the first two spatial POD modes appear to be the primary influence on the POD for the full line of sight. This also means that any discrepancy between the modeled and experimental free-stream conditions, such as high levels of free-stream turbulence, could significantly affect the prediction of wavefront POD modes if it disrupts the shock structure. It is difficult to draw hard conclusions only from the spatial modes. However, it is clear that the contribution from the shock and cavity zones is important to the overall aero-optics of this problem, and that even after removing the jitter caused by bulk shear layer oscillation, modeling this problem as a simple mixing layer is insufficient from the aero-optical point of view.

4.6 Dynamic Mode Decomposition of OPD

POD analysis can be useful as a means of data comparison and for identifying spatial modes, but does not necessarily give insight into the dynamics of a system. Several recent aero-optics studies [20] have used Dynamic Mode Decomposition (DMD) to analyze the spectral behavior of flows. Unlike POD, DMD provides a modal breakdown of the data where each basis function is tied to a single frequency. This is of obvious use in the analysis of systems driven by discrete forcing frequencies, such as the Rossiter modes in a cavity flow. In theory, DMD would allow the isolation of flow dynamics that occur at the key frequencies.

The standard DMD algorithm as given in Hemati, et al. [22] is as follows: as with POD, we compile a matrix of snapshot vectors $\mathbf{X} = [\mathbf{x}_1, \mathbf{x}_2, \ldots, \mathbf{x}_{N-1}]$. A second, offset snapshot matrix is formed such that $\mathbf{Y} = [\mathbf{x}_2, \mathbf{x}_3, \ldots, \mathbf{x}_N]$. The first snapshot matrix undergoes singular value decomposition,

$$\mathbf{X}' = \mathbf{Q}_X \mathbf{\Sigma} \mathbf{V}' \tag{20}$$

After which, the DMD operator matrix is constructed:

$$\tilde{\mathbf{K}} = \mathbf{Q}'_X \mathbf{Y} \mathbf{X}^+ \mathbf{Q}_X = \mathbf{Q}'_X \mathbf{Y} \mathbf{V} \mathbf{\Sigma}^{-1} \tag{21}$$

where $\mathbf{X}^+$ is the Moore-Penrose pseudoinverse of $\mathbf{X}$. The DMD modes and frequencies are then given by the eigenvectors and eigenvalues of $\tilde{\mathbf{K}}$, such that if $\mathbf{v}_j$ is the jth eigenvector with eigenvalue λ_j then $\mathbf{Q}_X \mathbf{v}_j$ is the jth DMD mode with frequency $f_j = imag(\log(\lambda_j))/2\pi\Delta t$ with Δt being the time interval between successive snapshots.

In this work, an alternative 'streaming' DMD algorithm developed by Hemati, et. al [22] is used. Instead of constructing the snapshot matrices in a single pass, the algorithm appends a single pair of snapshots to the system at a time, updating the basis sets $\mathbf{Q}_X$ and the corresponding $\mathbf{Q}_Y$ as snapshots are added. Limiting the ranks of the basis sets enables POD compression of the data set, which reduces noise in the snapshot data and allows the algorithm to pick out a small number (equal to the specified rank) of 'key' modes important to the system dynamics, rather than a full spectrum of modes. This is advantageous in the current problem because the limited time frame of the data collection and high levels of noise makes dominant modes very difficult to identify solely based on their magnitude. However, it does introduce uncertainty since the calculated modes are sensitive to the choice of maximum rank. Presently, the maximum rank of the DMD operator was set to 50, which was sufficient to isolate all of the larger peaks in the OPD spectra along the optical beam path.

The DMD was applied to snapshots of OPD spanning the entire cavity, which were sampled at 24 kHz. The total sample size was 215 snapshots. The choice of the larger aperture size serves to better give an idea of the overall flow dynamics which govern the OPD over the cavity, rather than a small sample at the cavity center. Furthermore, it is not guaranteed that the 3cm aperture of the beam is large enough to capture the largest aero-optical structures in the flow. As before, the flow was split into three distinct vertical regions spanning the recirculation zone in the cavity, the shear layer, and the shock region above the cavity. Figure 16 compares the spectra of the computed DMD modes with an average OPD power spectral density over the optical beam path. It should be noted that the OPD spectra over the full cavity do not necessarily match those over the smaller aperture; the latter were used mostly because they were sampled at a higher frequency of 106 kHz and thus confirmed that the detected peaks above 10 kHz were not solely due to aliasing.

The shock region spectra (Figure 16a) show distinct peaks at the third, fourth, and fifth Rossiter modes (with the third mode being dominant), as well as a peak around 11 kHz before a rapid drop-off in intensity occurs at higher frequencies. The dominant modes computed by the streaming DMD algorithms cluster near the Rossiter modes and the 11 kHz peak. The shear layer spectra (Figure 16b) displays a much more uniform distribution of energy, with a higher relative PSD at frequencies into the tens of kilohertz. Relative peak intensities are seen at the first five Rossiter modes. The DMD produced peaks close to the Rossiter modes as well as a largely uniform clustering between 5.5 and 11 kHz. In contrast, the recirculation region spectra (Fig. 16c) are dominated by the lower frequencies, with dominant peaks at the first two Rossiter modes as well as a frequency in between.

The real components of the main DMD modes for each of the flow regions are presented in Figures 17-19. The black circle on each mode shows the location of the optical beam for reference. Overall, the shock region exhibits the smoothest and most coherent optical structures

in the form of regular waves spanning the cavity which increase in magnitude as they travel downstream and decrease in wavelength at higher frequencies. These mode shapes roughly correspond with the shear layer modes (Figure 18) at similar frequencies, although the latter are a lot noisier. The structural similarity is consistent with the formation process of the shocklets above the cavity, which occur when the shear layer deflects into the free-stream. Thus the aero-optical structures in the shock region assume the shape of the larger-scale oscillations of the shear layer and propagate them into the free-stream above the cavity. In essence, the shock region structures are an inviscid footprint of the ones in the shear layer. This relationship could factor into the design of an effective adaptive optics system for supersonic cavity flows - namely, a configuration which reduces the aero-optical aberrations due to shear layer oscillation at the Rossiter frequencies would at the same time potentially counteract the aberrations caused by the shock region.

The dominant modes in the recirculation region (Figure 19), on the other hand, show less uniform behavior. The lowest-frequency mode appears almost like a standing wave spanning the entire length of the cavity. Near the second, third, and fourth, Rossiter modes (f_2, f_3, and f_4) there is an apparent split at the cavity midpoint. In the downstream half of the cavity, the modes show large structures with high intensity that do not span the cavity width and are due either to the impingement of the shear layer on the rear cavity wall or vortices caused by large structures in the shear layer entraining air from the recirculation region. In the upstream half of the cavity, the mode shapes resolve into relatively faint bar structures indicative of upstream-traveling pressure waves. At the highest detected frequency ($f_5 = 9.390$ kHz), the DMD mode consists of isolated structures that shrink downstream. The physical process behind these is not immediately obvious but could be due to the influence of convecting structures in the shear layer.

5.0 CONCLUSIONS

In this study, a hybrid LES/RANS methodology was applied to a high Reynolds number supersonic open cavity flow with an optical aperture, with the driving motivation being to confirm that the low-dissipation LES/RANS approach can provide accurate simulation of the small-scale, transient, turbulent effects that have a large impact on the performance of optical systems. The simulation showed good agreement with Schlieren photography from the experiment and the shear layer oscillation was well-predicted by Rossiter's empirical formula. The root mean square OPD was over-predicted by approximately 10% in the simulation. The proper orthogonal modes of the wavefront distortion compared very well with the experimental data with the exception of a prominent spatial structure seen in the experiment, which may be due to wind tunnel noise. Despite prior studies[7] suggesting anomalous behavior in
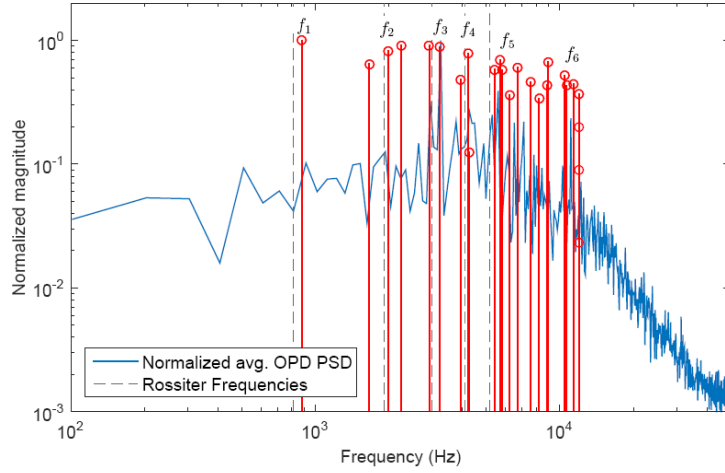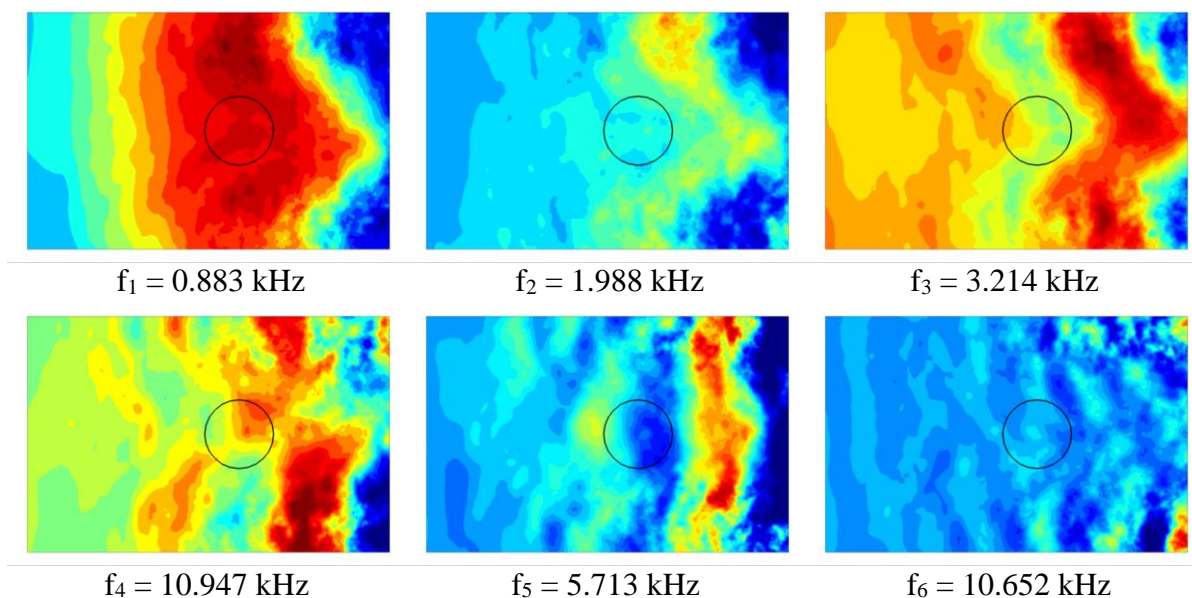
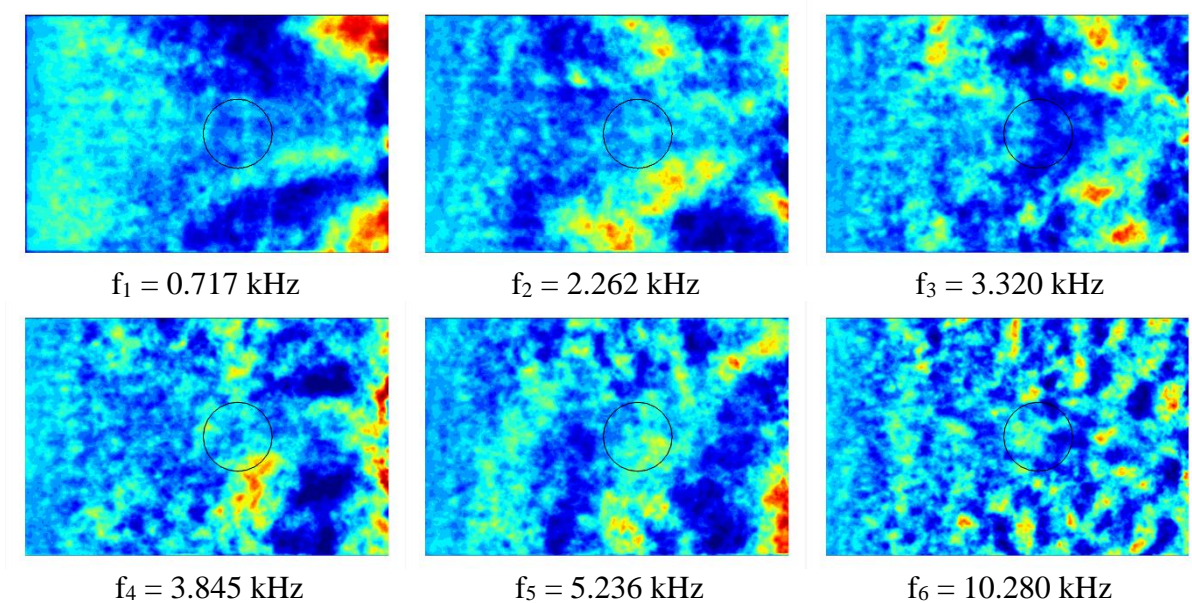(a) Shock region
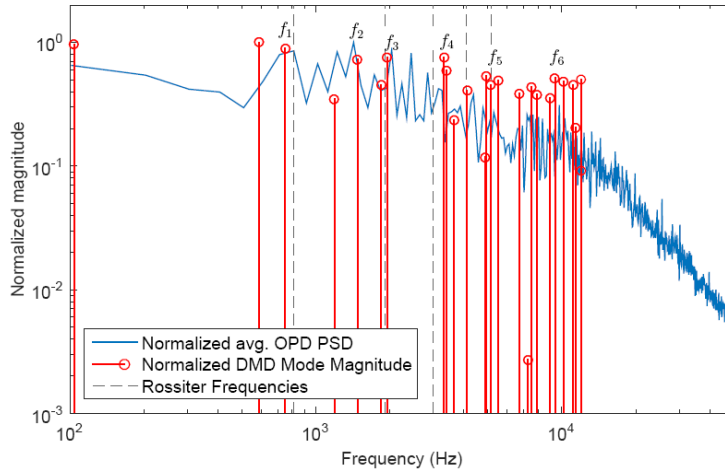
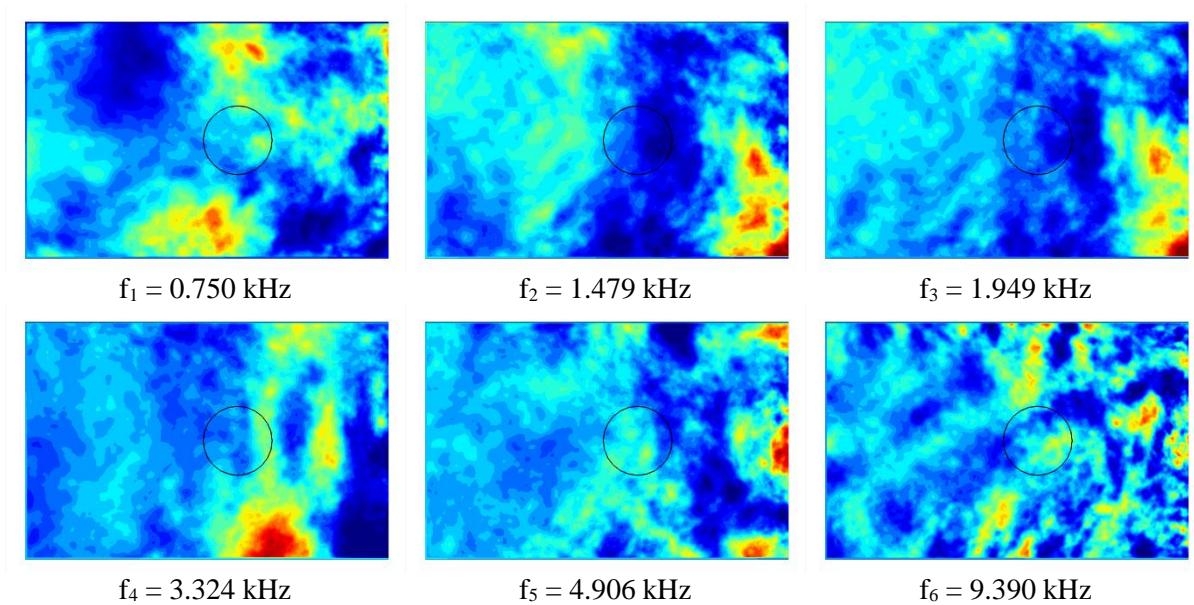(b) Shear layer region
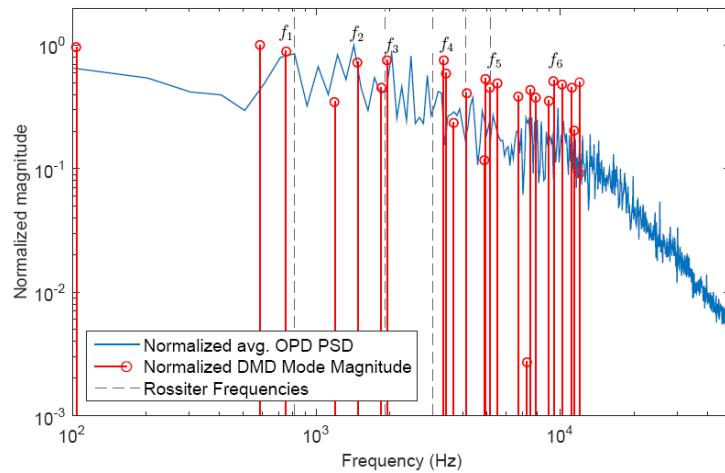
(c) Cavity recirculation region

Figure 16. Comparison of DMD mode frequencies and aperture-averaged OPD spectra

f₁ = 0.883 kHz   f₂ = 1.988 kHz   f₃ = 3.214 kHz

f₄ = 10.947 kHz   f₅ = 5.713 kHz   f₆ = 10.652 kHz

Figure 17. Full-cavity shock region DMD modes

f₁ = 0.717 kHz   f₂ = 2.262 kHz   f₃ = 3.320 kHz

f₄ = 3.845 kHz   f₅ = 5.236 kHz   f₆ = 10.280 kHz

Figure 18. Full-cavity shear layer region DMD modes

f₁ = 0.750 kHz	f₂ = 1.479 kHz	f₃ = 1.949 kHz
$f_1 = 0.750$ kHz	$f_2 = 1.479$ kHz	$f_3 = 1.949$ kHz
$f_4 = 3.324$ kHz	$f_5 = 4.906$ kHz	$f_6 = 9.390$ kHz

Figure 19. Full-cavity recirculation region DMD modes

the boundary layer over the wind tunnel window, computed POD modes and *rms* OPD of the simulated boundary layer were in close agreement. Overall, the results suggest that an LES/RANS approach is sufficiently robust to accurately model aero-optical aberrations, even for non-idealized flows.

A further decomposition of the cavity flow into distinct regions showed that while the shear layer spanning the cavity was responsible for the bulk of the aero-optical distortions, the region of shock waves caused by shear layer entrainment into the free-stream also produced a significant contribution, and was responsible for some of the coherent structure seen in the POD of the wavefront. A dynamic mode decomposition of a much larger wavefront spanning the entire cavity was performed and showed that the main driver of aero-optical aberrations is the bulk flapping motion of the shear layer occurring at the Rossiter frequencies. The oscillation causes a similarly-shaped wavefront distortion within the shock layer region over the cavity. At lower frequencies, the structures larger than the aperture of the Shack-Hartmann sensor used to measure OPD in the experiment, so a significant aperture-size effect is to be expected.

There are several uncertainties left to explore regarding the use of LES/RANS models to simulate aero-optics problems. Foremost, while it is assumed that the significant aero-optical aberrations occur in the free-stream, the actual effect of the near-wall RANS model choice and blending function has not been studied. A related problem is with the modeling of flow near the wall with the immersed boundary method. Although in the present case the assumption that the flow developing upstream of the cavity is fully turbulent appeared to produce adequate results, this is far from a safe assumption. For example, if the point of interest was aero-optical distortions over the flat plate upstream of the cavity, the precise IB wall model would certainly be consequential. Nevertheless, if the near-wall modeling is handled in a careful way, the IB methodology coupled with LES/RANS is potentially attractive for simulating flows over more complicated geometries, such as optical turrets.

6.0 CONNECTIONS

7.0 ACKNOWLEDGEMENTS

8.0 REFERENCES

[1] Wang H., Sun, M., Qin N., Wu H., Wang Z., "Characteristics of Oscillations in Supersonic Open Cavity Flows." *Flow, Turbulence, and Combustion,* Vol. 90, No.1, pp 121-142. 2013.

[2] Peng, S.H. and Liecher, S. "DES and Hybrid RANS-LES Modelling of Unsteady Pressure Oscillations and Flow Features in a Rectangular Cavity." Adv. In Hybrid RANS-LES Modelling, NNFM 97, pp.132-141, 2008.

[3] Mani A., Wang M., and Moin, P. "Resolution Requirements for Aero-optical Simulations." *J Computational Physics*, Vol. 227, 2008, pp 9008-9020

[4] Wang M., Mani A., and gordeyev S. "Physics and Computation of Aero-Optics." *Annu. Rev. Fluid Mech* Vol. 44, 2012, pp. 299-331

[5] Morgan, P. and Visbal, M. "Large Eddy simulation of flow over a flat-window cylindrical turret with passive flow control." *48th AIAA Aerospace Sciences Meeting*, 2010

[6] Engfer C., Pfuller E., and Wiedemann M. "Evaluation of the Aero-Optical Properties of the SOFIA Cavity by Means of Computational Fluid dynamics and a Super Fast Diagnosatic Camera." *Proceedings of SPIE*, 2012

[7] Smith A.E, Gordeyev S, Ahmed H, Ahmed A, Wittich D. J, and Paul M. "Shack-Hartmann Wavefront Measurements of Supersonic Turbulent Boundary Layers in the TGF." 45th AIAA Plasmadynamics and Lasers Conference, 16-20 June 2014.

[8] Edwards, J.R. "A Low-Diffusion Flux-Splitting Scheme for Navier-Stokes Calculations," *Computers and Fluids*, Vol. **26**, No. 6, 1997, pp. 635-659.

[9] Ducros, F., Ferrand, V., Nicaud, F., Weber, C., Darracq, D., Gachareiu, C., Poinsot, T. "Large-Eddy Simulation of the Shock / Turbulence Interaction" *Journal of Computational Physics*, Vol. **152**, No. 2., 1999, pp. 517-549.

[10]Gieseking, D.A., Choi, J.-I., Edwards, J.R., and Hassan, H.A. "Compressible Flow Simulations using a New LES/RANS Model" *AIAA Journal,* Vol. 49, No. 10, 2011, pp. 2194-2209.

[11] Choi, J-I., Oberoi, R.C., Edwards, J.R., and Rosati, J.A. "An Immersed Boundary Method for Complex Incompressible Flows", *Journal of Computational Physics,* Vol. 224, 2007, pp. 757-784.

[12] Edwards, J.R., Choi, J.-I., Ghosh, S., Gieseking, D.A., and Eischen, J.W. "An Immersed Boundary Method for General Flow Applications," 2010 ASME Fluids Engineering Meeting and Exhibits, Aug 1-4, 2010.

[13] Ghosh, S., Choi, J-I., and Edwards, J.R. "Numerical Simulations of the Effects of Micro-Vortex Generators using Immersed Boundary Methods" *AIAA Journal,* Vol. 48 No. 1, 2010, pp. 92-103.

[14] Rossiter, J. E., "Wind-Tunnel Experiments on the Flow Over Rectangular Cavities at Subsonic and Transonic Speeds," Aeronautical Research Council, Reports & Memoranda No. 3438, London, England, Oct. 1964.

[15]Wang H., Sun M., Qin N., Wu H., and Wang, Z. "Characteristics of Oscillations in Supersonic Open Cavity flows." *Flow Turbulence Comustion*, 2012

[16] Zhang X. and Edwards J. "An Investigation of Supersonic Oscillatory Cavity Flows Driven by Thick Shear Layers". *Aeronautical Journal of the Royal Aeronautical Society*, 1990, pp. 355-364

[17] Vogel C, Taylor G, and Wittich D. "Spatial-Temporal-Covariance-based Modeling, Analysis, and Simulation of Aero-Optics Wavefront Aberrations." *Journal of the Optical Society of America* Vol. 37, No. 7, 2014, pp. 1666-1679

[18] Arunatajesan S. and Sinha N. "On the Application of Hybrid RANS-LES and Proper Orthogonal Decomposition Techniques to Control of Cavity Flows." *Proceedings of the third AFOSR International Conference on DNS/LES*, 2000

[19] Sirovich, L. "Turbulence and the dynamics of coherent structures." I—III. Quart. Appl. Math., 45(3):561–590, 1987.

[20] Goorskey D., Drye R., and Whiteley M. "Dynamic Modal Analysis of Transonic Airborne Aero-Optics Laboratory Conformal Window Flight-Test Aero-Optics." *Optical Engineering* Vol 52, No 7, 2013

[21] Goorskey D., Whiteley M., Gordeyev S., and Jumper E. "Recent In-Flight Wavefront Measurements of Aero-Optics and Implications for Aero-Optics Beam Control in Tactical Laser Weapons Systems." *42nd AIAA Plasmadynamics and Lasers Conference*, 2011.

[22] Hemati M, Williams M., and Rowley C. "Dynamic mode decomposition for large and streaming datasets." *Physics of Fluids* Vol. 26, 2014

DISTRIBUTION LIST

DTIC/OCP
8725 John J. Kingman Rd, Suite 0944
Ft Belvoir, VA 22060-6218   1 cy

AFRL/RVIL
Kirtland AFB, NM 87117-5776   1 cy

John Tam
Official Record Copy
AFRL/RDLE   1 cy